Engineering 23 (2023) 149–156

Contents lists available at ScienceDirect

Engineering

journal homepage: www.elsevier.com/locate/eng

Research
Water Pollution Control—Article

Commercial Gel-Type Ion Exchange Resin Enables Large-Scale Production of Ultrasmall Nanoparticles for Highly Efficient Water Decontamination

Sikai Cheng [a], Jieshu Qian [b], Xiaolin Zhang [a,c,*], Zhenda Lu [c,d], Bingcai Pan [a,c]

[a] School of Environment, Nanjing University, Nanjing 210023, China
[b] School of Environmental and Biological Engineering, Nanjing University of Science and Technology, Nanjing 210094, China
[c] Research Center for Environmental Nanotechnology (ReCENT), Nanjing University, Nanjing 210023, China
[d] College of Engineering and Applied Science, Nanjing University, Nanjing 210023, China

ARTICLE INFO

Article history:
Received 16 May 2021
Revised 26 August 2021
Accepted 1 September 2021
Available online 18 November 2021

Keywords:
Nanoscale effect
Nanoconfinement
Adsorption
Inner-sphere complex
Regeneration

ABSTRACT

Nanotechnology presents innovative solutions in advanced water treatment; however, its application is limited by the challenging large-scale production of ultrasmall (< 5 nm) nanoparticles (NPs) with extraordinary decontamination reactivity and the difficulty of handling such tiny NPs in engineering. To address these challenges, we propose a straightforward route for synthesizing ultrasmall NPs using the commercial gel-type anion exchange resin N201 as the host. N201 is a millimeter-scale poly(styrene-*co*-divinylbenzene) bead modified with quaternary ammonium groups. Nanoparticles of hydrated ferric oxide (HFO), hydrated manganese oxide (HMO), cadmium sulfide (CdS), and zero-valent iron (ZVI) were obtained through simple impregnation–precipitation in N201, and all of the NPs possessed an ultrasmall size of sub-5 nm. A pilot-scale production assay indicated that the synthetic system could be enlarged proportionally to prepare massive sub-5 nm HFO. Regarding the underlying mechanism, each N201 bead contained a continuous water phase, allowing the rapid diffusion of the reactants (7 s for diffusion from the bead surface to the center), resulting in burst nucleation to produce ultrasmall NPs with a narrow size distribution. Moreover, the crosslinked polymer chains provided a confined space (< 5 nm diameter) to prevent the excessive growth of the formed NPs. Owing to the millimetric N201 host, the resultant nanocomposite can be applied in flow-through systems. The batch and column adsorption assays demonstrate the dramatically enhanced adsorption performance of the ultrasmall HFO toward As(III/V) than the ~17 nm analogs. This study can advance the widespread use of nanotechnology in practical water treatment.

1. Introduction

Several inorganic pollutants, including arsenic (As), heavy metals, phosphorus (P), and fluorine (F), negatively impact human health and the ecosystem, even when present in the human body or the environment at trace levels [1–4]. Reducing these pollutants to sub-milligram per liter concentration levels under economically acceptable conditions is difficult [5–8]. Over the past several decades, the rapid development of nanotechnology has offered a new opportunity for process innovation in advanced water treatment [9–12]. Owing to their high specific surface area, nanoparticles (NPs) exhibit significantly enhanced adsorptive/catalytic reactivity than the bulky analogs [13–16]. Particularly, the (hydro)oxides of Fe(III), Mn(IV), Zr(IV), and zero-valent iron (ZVI) have attracted much attention in water pollution control, because of their capability to form inner-sphere complexes with heavy metals, fluoride, and oxyanions [17–20].

The direct utilization of NPs in water treatment is impractical. The drawbacks mainly include the tendency of NPs to aggregate in water, difficulty in handling NPs, and potential risk caused by the released NPs [21–23]. To address these problems, NPs are often encapsulated inside bulky host materials through the impregnation–precipitation method [24,25]. For instance, millimeter-scale macroporous resin beads have been used as hosts

* Corresponding author.
E-mail address: XLZhang@nju.edu.cn (X. Zhang).

https://doi.org/10.1016/j.eng.2021.09.010

to accommodate various NPs, and the resultant nanocomposite materials can be steadily used in flow-through systems owing to their excellent hydraulic performance and high mechanical strength [22]. The crosslinked polymer chains can act as a cage to avoid NP leaching from the hosts [26,27], providing the nanocomposite materials with outstanding stability. Interestingly, in previous research, some polymer nanocomposites used in the pilot-scale treatment of industrial effluents exhibited exceptional stability during a two-year successive fixed-bed run [28,29].

The adsorption reactivity of NPs is highly dependent upon their size [30–33]. With decreasing particle size, the specific surface area increases accordingly, providing more sites for adsorption. More importantly, much more constitutional atoms are exposed to the surface when the particle size decreases to an ultrasmall level (e.g., < 5 nm), and the proportion of the highly reactive sites considerably increases [33,34]. In a previous study, decreasing Fe_3O_4 size from 300 to 12 nm led to a 12-fold increase in adsorption capacity toward As(III/V), reducing the residual arsenic concentration from hundreds of microgrammes per liter to several microgrammes per liter [32]. Similarly, our previous study found that the normalized adsorption capacity of 2 nm α-FeOOH particles was 14.8 times that of 18 nm × 60 nm particles [33].

Burst nucleation is a crucial step in the aqueous-phase synthesis of ultrasmall NPs [35–37]. It requires a rapid reaction between the metallic precursors and the precipitants to generate a high supersaturation level, causing an explosive increase in the number of nuclei and the rapid consumption of the active monomers [38]. Given that the activation energy for nucleation is much higher than that for crystal growth, the nucleation reaction only persists for a short duration and stops at a supersaturation level that is still high enough for the growth reaction [39,40]. Thus, the nucleation and growth processes are temporally separated, and all of the particles have almost the same growth history, enabling the formation of ultrasmall NPs with narrow size distribution. Organic surfactants are often used to prevent NP aggregation or further growth, as the excess surfactants bind to the nanocrystal surface sites [41–43]. However, burst nucleation hardly occurs inside the bulky hosts because the retarded diffusion kinetics makes the sudden increase in supersaturation level difficult [44]. Moreover, considering the difficulty in the precise size control of the host pores, without the stabilization of organic surfactants, the NP is expected to further grow [45,46].

In this study, we report a straightforward strategy to prepare ultrasmall NPs through impregnation–precipitation in a commercial gel-type anion exchange resin N201. N201 is a poly(styrene-*co*-divinylbenzene) bead (0.6–0.8 mm diameter) modified with quaternary ammonium groups. Since its first synthesis in the 1940s, N201 has been widely used in water softening, water purification, and radioactive element separation [47,48]. In this study, we demonstrated that when swollen in water, N201 contains a continuous water phase as the major component (~55% in mass) to allow the fast diffusion of the reactants. The reactant required 226 s to diffuse from the bead surface to the center of D201 (a macroporous anion exchange resin), whereas the diffusion time for N201 was 7 s. Thus, N201 exhibits a rapid increase in the supersaturation level to initiate burst nucleation. Meanwhile, the crosslinked matrix of N201 limits the diameter of the swollen pores to < 5 nm [49], providing physical confinement to prevent the further growth of the generated NPs. Thus, we obtained several sub-5 nm particles, namely hydrated ferric oxide (HFO), hydrated manganese oxide (HMO), cadmium sulfide (CdS), and ZVI. The potential of this new synthesis method for large-scale production was verified through the synthesis of 20 kg of HFO@N201 nanocomposite. Moreover, we investigated the possible use of the resultant ultrasmall NPs for water decontamination, verifying their superior adsorption reactivity toward arsenic than the ~17 nm analogs.

2. Materials and methods

2.1. Nanocomposite preparation

N201 and D201 were purchased from Zhengguang Industrial Co., Ltd. (China). The details of the N201 and D201 structures are presented in Table S1 in Appendix A. The macroporous nanocomposite HFO@D201 was prepared according to previous studies [50,51]. First, 20 g of dry D201 beads were added into a 400 mL solution containing 0.8 mol·L^{-1} of $FeCl_3$ and 1.5 mol·L^{-1} of HCl. After the solution was stirred at room temperature for 6 h, the beads were filtered out and then added into a binary 400 mL NaOH–NaCl (5:5, w/w) solution for the *in situ* precipitation of HFO NPs. The NPs were then rinsed several times with pure water and subjected to thermal treatment at 333 K for 6 h to obtain the resultant HFO@D201. The gel-type nanocomposite HFO@N201 was prepared through the same method, except that N201 was used as the host material. Appendix A Text S1 describes the synthesis details for the other gel-type nanocomposites, including ZVI@N201, HMO@N201, and CdS@N201.

2.2. Batch adsorption

The solid nanocomposites were introduced into the As(III/V) solutions to evaluate the decontamination capability. The HFO@D201 and HFO@N201 dosages were set as 0.3 g·L^{-1}, unless otherwise stated. The resultant solutions were shaken at 298 K for 48 h to reach adsorption equilibrium, after which the residual arsenic concentration was determined to calculate the As(III/V) uptake amount. Throughout the experiments, HCl (0.10 mol·L^{-1}) and NaOH (0.10 mol·L^{-1}) solutions were used to maintain the solution pH at the preset values.

2.3. Column adsorption

Fixed-bed adsorption experiments were performed in glass columns (240 mm length and 14 mm diameter) with water bath jackets to maintain a constant temperature of 298 K. Each column was packed with 5 mL solid adsorbents. The synthetic feeding solution containing As(III/V) and other coexisting substances (e.g., SO_4^{2-}, Cl^-, HCO_3^-, NO_3^-) was pumped up-to-down through the column using a peristaltic pump (LongerPump BT01-100, China) at a constant flow rate, and the empty bed contact time was set as 3 min, equivalent to 20 bed volumes (BV) per hour.

2.4. Characterization and analysis

The NP crystalline structure was determined using an X-ray diffraction (XRD) analyzer (ARL X'TRA, Switzerland) over a wide range of angles (5°–80°). The surface area and pore structure of D201, HFO@D201, and the dry N201 were determined via N_2 adsorption–desorption tests, performed at 77 K using a micropore analyzer (Autosorb-IQ-MP, Quantachrome, USA). The elemental Fe distribution along the nanocomposite beads was analyzed via scanning electron microscopy (Hitachi S-3400N II, Japan) coupled with energy-dispersive spectroscopy (SEM–EDS). The NP microscopic structure was obtained via transmission electron microscopy (TEM; Tecnai F20, FEI, USA), and high-angle annular dark-field (HAADF) images were obtained through scanning TEM (STEM). Moreover, X-ray photoelectron spectroscopy (XPS) measurements with a monochromatic Al Kα radiation source (1486.6 eV, 1 eV = 1.6 × 10^{-19} J) were performed on a PHI5000 VersaProbe system (ULVAC, Japan). Potentiometric titration measurements were performed using an automatic titration system

(T50, Mettler Toledo, Switzerland) equipped with a combined glass pH electrode (DGi115-SC, Mettler Toledo).

The Fe(III) concentration was obtained via inductively coupled plasma–optical emission spectrometry (iCAP 7400, Thermo Fisher Scientific, USA), and the arsenic concentration was determined via inductively coupled plasma–mass spectrometry (ICP–MS; NexION 300X, PerkinElmer, USA).

3. Results and discussion

3.1. Synthesis of ultrasmall NPs

To clarify the advantages of N201 for ultrasmall NP synthesis, we used N201 and D201 as hosts for the HFO NPs. Both N201 and D201 were fabricated from the suspension copolymerization of styrene and divinylbenzene, followed by chloromethylation and quaternary ammoniation [52–54]. The only difference was that isobutanol was used as the porogen to mix with styrene and divinylbenzene in the copolymerization stage for D201, and permanent nanopores were formed in the resultant beads after the extraction of isobutanol [55]. According to the pore size distribution of the dry N201 and D201 based on N_2 adsorption–desorption tests, N201 exhibited negligible permanent pores, while D201 exhibited abundant nanopores with a broad size distribution of 1–80 nm (Appendix A Fig. S1).

To obtain the nanocomposite adsorbents (HFO@N201 and HFO@D201), $FeCl_4^-$ complex anions were used as the inorganic precursors, and they were impregnated into N201 and D201 through electrostatic attraction with quaternary ammonium groups. Afterward, the beads were immersed in an alkali solution to produce HFO NPs. The impregnation of $FeCl_4^-$ and HFO NPs into the N201 beads had negligible effects on their shape but changed their color from transparent to brown and black, respectively (Fig. 1(a)). In contrast, the impregnation of HFO NPs into D201 changed its color from white to reddish-brown (Appendix A Fig. S2). After acid digestion, the iron contents in HFO@N201 and HFO@D201 were determined as 9.97% ± 0.10% and 9.93% ± 0.04%, respectively. The XRD patterns suggest that the main phases in both samples were poorly crystallized ferrihydrite (Appendix A Fig. S3) [56]. Furthermore, as shown in the TEM and STEM–HAADF images, the NPs inside HFO@N201 (Figs. 1(b) and (c)) occurred as much smaller clusters than those inside HFO@D201 (Appendix A Figs. S2(b) and (c)). Based on the statistical analysis of 200 particles randomly selected from the TEM image of each sample, we determined the average NP size in HFO@N201 and HFO@D201 as (2.51 ± 0.71) and (17.61 ± 7.79) nm, respectively. Representative SEM–EDS images showed that HFO NPs were distributed uniformly in HFO@N201 (Appendix A Fig. S4), suggesting that the HFO NP nucleation occurred uniformly inside the N201 bead, as discussed below.

Other inorganic particles, including HMO, CdS, and ZVI, were also prepared using N201 as the host. The obtained NPs exhibited an ultrasmall size of < 5 nm (Appendix A Figs. S5(a)–(c)). Furthermore, 20 kg of HFO@N201 was produced by enlarging the synthetic system proportionally, and the resultant HFO NPs still possessed a small particle size of (3.72 ± 0.95) nm (Figs. S5(d) and (e) in Appendix A).

3.2. Underlying mechanism for ultrasmall NP formation

Appendix A Fig. S6 shows that the $FeCl_4^-$ precursors were uniformly distributed in D201 and N201. After acid digestion, the loadings of $FeCl_4^-$ in D201 and N201 were both determined as approximately 2.0 mmol·g^{-1}. The diffusion of the precipitant (i.e., OH^- ions) inside the beads may be responsible for the formation of ultrasmall NPs inside N201. To monitor the diffusion of OH^- ions, the N201 and D201 beads were immersed in phenolphthalein solution, and one drop of NaOH solution (1 mol·L^{-1}) was added to the phenolphthalein-preloaded D201/N201. Given that phenolphthalein immediately turns red upon reacting with OH^- ions, the diffusion of OH^- ions inside N201 and D201 could be visualized by the color change in the cross-section of each bead. As depicted in Fig. 2(a), the OH^- ion diffusion inside N201 was fast, and the ions reached the bead center within 7 s. In contrast, the OH^- ions required approximately 226 s to reach the D201 bead center. The rapid diffusion of the precipitants allows a sudden increase in the supersaturation level inside N201, so that burst nucleation commences, and tiny NPs are produced. Regarding the underlying

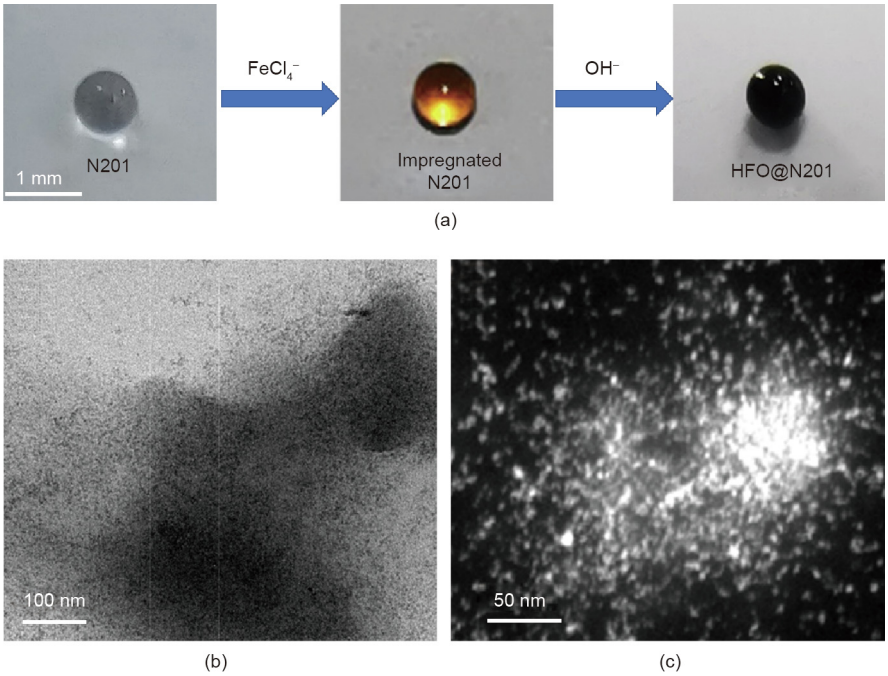

Fig. 1. (a) Optical photos of N201, $FeCl_4^-$-preloaded N201, and HFO@N201; (b) TEM and (c) STEM–HAADF pictures of HFO@N201.

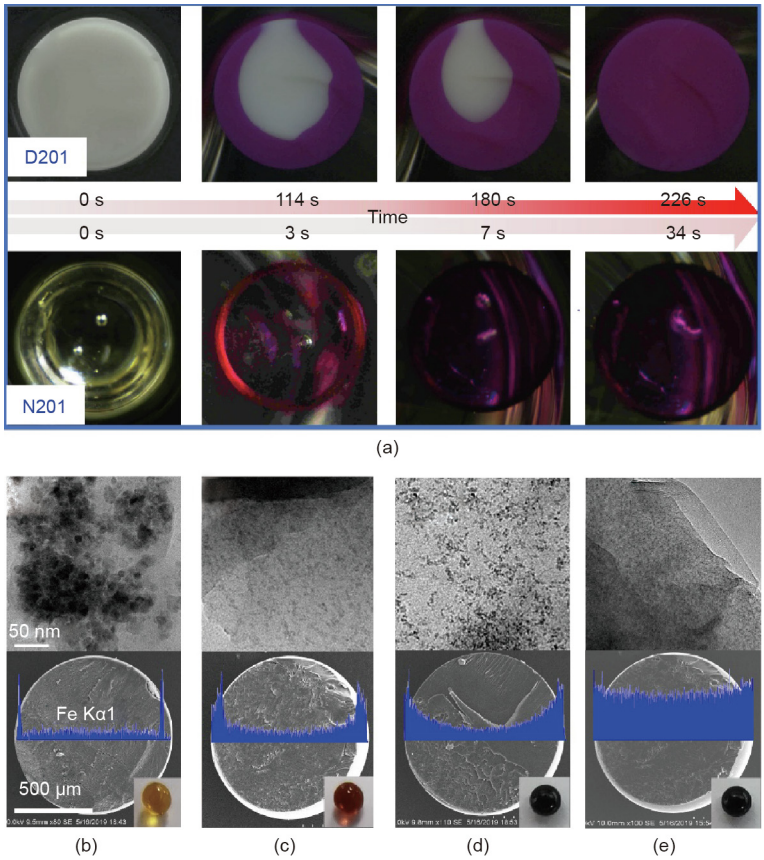

Fig. 2. (a) Optical photos of cross-section of the phenolphthalein-preloaded D201/N201 after contacting with NaOH solution droplet at time intervals, and (b)–(e) TEM pictures and elemental Fe distribution along the cross-section of the HFO@N201 samples prepared with varying NaOH concentration (inset is the optical photos of the HFO@N201 samples, and (b)–(e) correspond to 0.1%, 1%, 3%, and 5% NaOH solutions, respectively).

mechanism, when the N201 was swollen in water, its volume was enlarged by 1.8 times (Appendix A Fig. S7) owing to the solvation of polymer chains [49]. From mass balance, it is estimated that the swollen N201 contained a continuous water phase as its major component (~55% in mass). The diffusion resistance in the continuous water phase was much less than that in a rigid solid phase such as the D201 matrix [57,58], thus facilitating the rapid diffusion of OH^- ions inside N201.

Given that ion diffusion is initially driven by concentration gradient, we also examined the effect of the OH^- concentration on NP formation. When the $FeCl_4^-$-preloaded N201 beads were immersed in 0.1% NaOH solution, the HFO NPs were mainly distributed in the N201 peripheral section and possessed an average size of 14 nm (Fig. 2(b)), indicating the absence of burst nucleation. With the NaOH concentration increased to 5%, however, burst nucleation dominated the formation of FeOOH NPs, and massive 2.5 nm HFO NPs were uniformly distributed inside N201 (Figs. 2(c)–(e)). The change in the NP size and distribution also resulted in a significant change in the HFO@N201 color (Figs. 2(b)–(e) insets) despite the similar NP loading amounts (~10%) among the nanocomposite samples. These results further confirm the key role of fast diffusion in burst nucleation and ultrasmall NP formation.

Besides burst nucleation, the N201 pore structure may also play an important role in the formation of tiny NPs. As previously reported, the crosslinked polymer chains prevent the excessive swelling of N201 and restrict the pore size to < 5 nm [49]. Hence, the ultrasmall NPs formed through burst nucleation can be well stabilized by the tiny nanopores, preventing agglomeration or further growth. In contrast, burst nucleation commenced inside D201 when the $FeCl_4^-$-preloaded D201 beads were immersed in 10% NaOH solution; however, the formed HFO NPs still possessed a relatively large size of 15.4 nm (Appendix A Fig. S8) owing to the excess growth inside the macropores. The underlying mechanism of ultrasmall NPs synthesis is schematically illustrated in Fig. 3.

Ultrasmall NPs can be prepared using gel-type ion exchange resin as the host under mild conditions without the use of surfactants. The method proposed in this study is more suitable for large-scale production than the other widely used impregnation–precipitation methods owing to the promising properties of the gel-type ion exchange resin, such as cost effectiveness, commercial availability, chemical stability, and mechanical strength. However, because of the relatively poor stability against high temperature, the method may be unsuitable for the calcination-based synthesis of the well-crystallized NPs.

3.3. Adsorption reactivity toward As(III/V)

We compared the adsorption reactivities of HFO@N201 and HFO@D201 toward As(III/V). The batch experiments were performed at 298 K to obtain the adsorption isotherms. The preliminary study suggests that the N201 and D201 hosts exhibited negligible adsorption toward As(III) because of its electrical neutrality, and massive sulfate (2 $g \cdot L^{-1}$) was added into the solutions to screen the electrostatic attraction of the N201/D201 hosts with As(V). Hence, the adsorption of HFO@N201/HFO@D201 toward As(III/V) is ascribed to the embedded HFO NPs. The adsorption isotherms of HFO@N201 and HFO@D201 conform well to the Langmuir model (Eq. (1)):

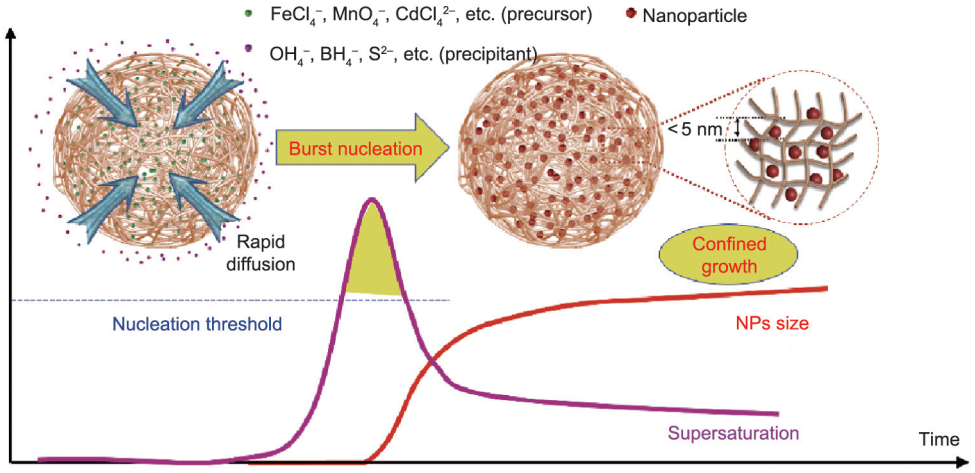

Fig. 3. Schematic illustration of the underlying mechanism for the formation of ultrasmall NPs inside N201.

$$Q_e = \frac{Q_m K_L C_e}{1 + K_L C_e} \quad (1)$$

where Q_e is the equilibrium adsorption capacity of As ($mg \cdot g^{-1}$); C_e is the equilibrium concentration of As in solution ($mg \cdot L^{-1}$); Q_m is the maximum As adsorption ($mg \cdot g^{-1}$); and K_L is the Langmuir adsorption isotherm coefficient. The K_L value can roughly reflect the adsorption affinity toward target pollutants. The Q_m and K_L values of HFO@N201 for both As(V) and As(III) were considerably higher than those of HFO@D201 (Figs. 4(a) and (b)). The Q_m and K_L values of HFO@D201 for As(V) were 98.4 $mg \cdot g^{-1}$ and 2.06 $L \cdot mg^{-1}$, respectively, whereas those of HFO@N201 were 229.2 $mg \cdot g^{-1}$ and 7.54 $L \cdot mg^{-1}$, respectively. The adsorption performance of the HFO@N201 prepared on a kilogram scale (Appendix A Fig. S9) was similar to that of the HFO@N201 prepared on a laboratory scale (Fig. 4(a)), as depicted by the adsorption isotherms.

The surface acid–base properties of HFO NPs inside HFO@N201 and HFO@D201 were detected through potentiometric titration analysis. Our preliminary study demonstrated that an N201/D201 host consumed negligible OH^- in the presence of 0.1 $mol \cdot L^{-1}$ of $NaNO_3$ at pH 3–11; thus, the consumed OH^- ions are attributed to the embedded NPs. The net surface charge Q_H values were calculated as described in Appendix A Text S2, and they were plotted as a function of pH (Fig. 4(c)). The Q_H values represent the net amount of H^+ ($Q_H > 0$) or OH^- ($Q_H < 0$) adsorbed on the NP surface. The absolute Q_H values of HFO@N201 were higher than those of HFO@D201, suggesting the occurrence of more protonation/deprotonation sites in HFO@N201. The deconvolution of the XPS O 1s

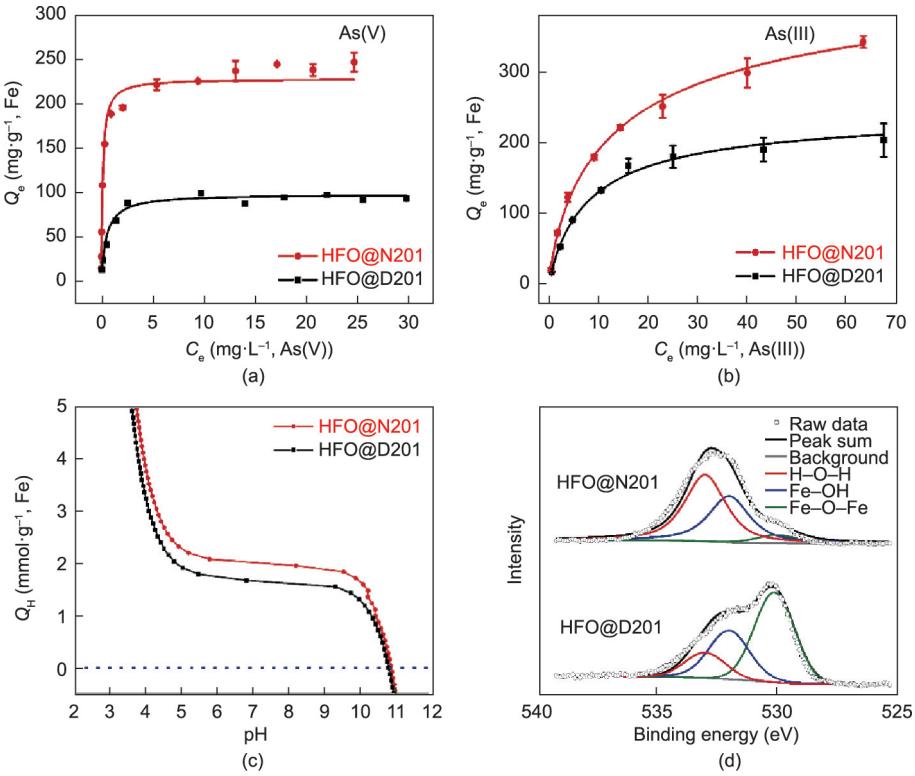

Fig. 4. Adsorption isotherms of (a) As(V) and (b) As(III) (solid dosage: 0.30 $g \cdot L^{-1}$; pH 7.0; T = 298 K); (c) net surface charge (Q_H) as a function of pH; (d) XPS O 1s spectra of HFO@N201 and HFO@D201.

spectra suggests that the surface oxygen of HFO NPs existed in three forms: lattice oxygen (Fe–O–Fe) with a binding energy of ~530 eV, terminal oxygen (Fe–OH) with a binding energy of ~532 eV, and coordinated water molecules (H–O–H) with a binding energy of ~533 eV [59]. Interestingly, HFO@N201 possessed a much lower proportion of the lattice oxygen (Fe–O–Fe) than HFO@D201 (Fig. 4(d)), owing to the ultrasmall nature of the NPs inside N201 [60]. The superior adsorption performance of HFO@N201 is mainly attributed to the much smaller NP size than that of HFO@D201, providing more active sites (i.e., the sum of Fe–OH and H–O–H) for adsorption (Fig. 4(d)). Both terminal oxygen (Fe–OH) and the coordinated water (H–O–H) were responsible for arsenic adsorption [61,62]. Moreover, the decreased proportion of the lattice oxygen (Fe–O–Fe) is consistent with the higher number of protonation/deprotonation sites in HFO@N201 than HFO@D201.

Furthermore, the adsorption performances of ultrasmall NPs toward various pollutants were investigated. The comparison of the adsorptions of phosphate by HFO@N201 and HFO@D201 (Appendix A Fig. S10) suggests a much higher adsorption capacity of HFO@N201 than HFO@D201. Similarly, compared with the NPs inside the macroporous ion exchange resin, the ultrasmall HMO inside the gel-type ion exchange resin exhibited superior adsorption capacities toward Ni(II) and As(V) (Fig. S10).

3.4. Potential for practical water treatment

In water treatment, coexisting anions compete with target pollutants for adsorption sites because of the structural similarity. The formation of inner-sphere complexes between HFO NPs and arsenic is barely influenced by common anions such as sulfate, chlorides, and nitrate [33,62,63]. As shown in Fig. 5(a), with the increase in the sulfate concentration to 50 mg·L^{-1}, the adsorption capacities of HFO@N201 and HFO@D201 declined owing to the suppression of the electrostatic attraction (i.e., ion exchange) of the N201 and D201 hosts. Nonetheless, HFO@N201 and HFO@D201 exhibited considerable adsorption capacities (220.4 and 94.7 mg·g^{-1}, respectively) even massive sulfate (2000 mg·L^{-1}) coexists. As shown in Appendix A Fig. S11, chloride and bicarbonate suppressed the adsorption capacities owing to the competition with As(V) for the electrostatic attraction sites in the N201 and D201 hosts. Silicate can also form inner-sphere complexes with iron oxide [64]; however, the affinity is much weaker than that between silicate and As(V) [65]. Thus, the presence of silicate (< 40 mg·L^{-1}) exerted negligible effects on As(V) adsorption onto HFO@N201 and HFO@D201. Furthermore, humic acid molecules with a relatively large size were difficult to diffuse inside the nanopores of the N201 and D201 hosts owing to size exclusion [66]; thus, their impact on the As(V) adsorption capacity was negligible. We determined the dissolution of HFO@N201 and HFO@D201 after immersion in the solutions with varying pH from 1 to 11 for 24 h. As illustrated in Appendix A Fig. S12, the negligible dissolution of HFO@N201 and HFO@D201 occurred at pH > 2, possibly owing to the protection of the nanoporous hosts [33]. With a further decrease in the pH to 1, the HFO@D201 dissolution increased to > 80%. In contrast, the HFO@N201 dissolution was ~25%, mainly because of the strong nanoconfinement effects posed by the ultrasmall nanopores of N201. After adsorption, HFO@N201 and HFO@D201 were refreshed by the binary NaOH–NaCl (5:5 w/w) solution. The HFO surface became negatively charged under alkaline conditions (pH > 10.8, Fig. 4(c)), thereby exerting strong electrostatic repulsion toward arsenic anions. Both HFO@N201 and HFO@D201 could be fully refreshed through alkaline treatment, and the removal efficiency toward arsenic remained constant during a seven-cyclic successive adsorption–regeneration assay (Fig. 5(b)). In addition, we determined the sphericity after the attrition of N201 and HFO@N201 before and after seven-cyclic adsorption–regeneration runs. The results in Appendix A Fig. S13 suggest that no pronounced difference occurred among the four samples (> 97%), verifying the satisfactory mechanical strength of N201 and HFO@N201. We used TEM and XRD to monitor the HFO NPs inside N201 before and after 60-day storage. The appearance and crystalline structure of the HFO NPs remained constant during the 60-day storage (Appendix A Fig. S14). The outstanding storage stability was possibly due to the physical confinement by the tiny nanopores of N201, preventing the agglomeration or further growth of the HFO NPs.

Furthermore, HFO@N201 and HFO@D201 were separately packed into glass columns to investigate their adsorption performance in flow-through mode (Fig. 6(a)). The simulated groundwater (see Figs. 6(b) and (c) for the basic parameters) was pumped up-to-down through the columns. The HFO@N201 column is capable of generating > 4800 BV clean water before As(V) concentration in the effluent exceeded 10 μg·L^{-1}. In contrast, this value was only ~1500 BV for the HFO@D201 column. The effective treatment amount of the N201 column was less than 50 BV (Fig. 6(b)) because the electrostatic attraction between N201 and As(V) was nonspecific, and the attraction was intensively inhibited by the coexisting anions. After utilization, the saturated HFO@N201 and HFO@D201 could be fully refreshed through alkaline treatment (Fig. 5(b)). Furthermore, the column adsorption performance toward As(III) (Fig. 6(c)) indicates that the HFO@N201 column could still generate 1200 BV clean water, whereas the HFO@D201 column could generate 400 BV.

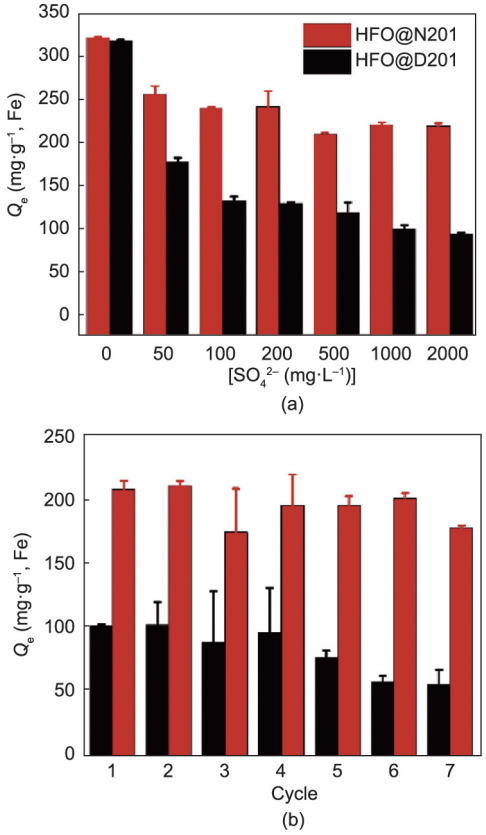

Fig. 5. (a) Effect of sulfate on As(V) removal by HFO@N201 and HFO@D201, and (b) cyclic adsorption–regeneration runs.

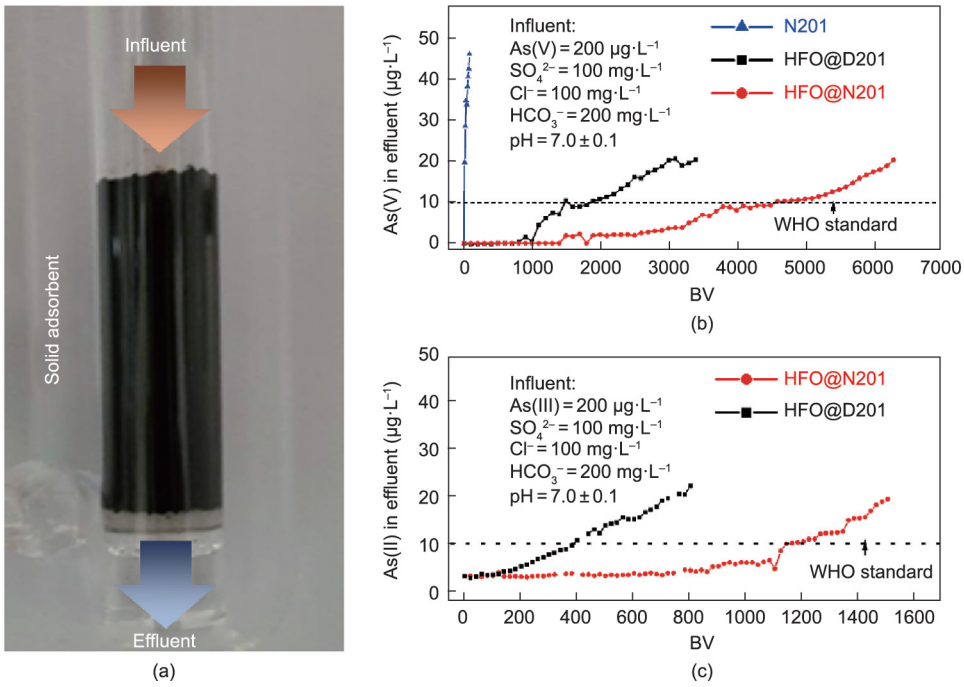

Fig. 6. Column adsorption of the simulated groundwater. (a) Photo of the column adsorption experiment, (b) treatment of the As(V) contaminated water, and (c) treatment of the As(III) contaminated water. The World Health Organization (WHO) recommended that the limit of arsenic in drinking-water is 10 μg·L^{-1} [50].

4. Conclusions

The large-scale synthesis of ultrasmall NPs of high decontamination reactivity is an attractive but challenging task in water pollution control. Herein, we report a general route for synthesizing sub-5 nm particles through simple impregnation–precipitation inside a commercial gel-type anion-exchange resin. Given the wide usage of gel-type anion-exchange resins in engineering and the frequent use of the impregnation–precipitation method for embedding metal(oxide) NPs inside bulky hosts, the proposed synthesis route may also be valid for other polymer nanocomposites. In summary, this study provides a potential route for the simple fabrication of ultrasmall NPs with extraordinary reactivity for environmental remediation and other applications.

Acknowledgments

We greatly appreciate the financial support from the National Natural Science Foundation of China (51878332, 21976084, and 21925602) and the Fundamental Research Funds for the Central Universities.

Compliance with ethical guidelines

Sikai Cheng, Jieshu Qian, Xiaolin Zhang, Zhenda Lu, and Bingcai Pan declare that they have no conflicts of interest or financial conflicts to disclose.

Appendix A. Supplementary data

Supplementary data to this article can be found online at https://doi.org/10.1016/j.eng.2021.09.010.

References

[1] Powley HR, Dürr HH, Lima AT, Krom MD, Van Cappellen P. Direct discharges of domestic wastewater are a major source of phosphorus and nitrogen to the mediterranean sea. Environ Sci Technol 2016;50(16):8722–30.
[2] Gao L, Gao B, Xu D, Peng W, Lu J. Multiple assessments of trace metals in sediments and their response to the water level fluctuation in the Three Gorges Reservoir, China. Sci Total Environ 2019;648:197–205.
[3] Tang W, Kovalsky P, He D, Waite TD. Fluoride and nitrate removal from brackish groundwaters by batch-mode capacitive deionization. Water Res 2015;84:342–9.
[4] Zhang Q, Bolisetty S, Cao Y, Handschin S, Adamcik J, Peng Q, et al. Selective and efficient removal of fluoride from water: *in situ* engineered amyloid Fibril/ZrO_2 hybrid membranes. Angew Chem Int Ed Engl 2019;58(18):6012–6.
[5] Song P, Yang Z, Zeng G, Yang X, Xu H, Wang L, et al. Electrocoagulation treatment of arsenic in wastewaters: a comprehensive review. Chem Eng J 2017;317:707–25.
[6] Ling C, Ren Z, Wei M, Tong F, Cheng Y, Zhang X, et al. Highly selective removal of Ni(II) from plating rinsing wastewaters containing $[Ni\text{-}xNH_3\text{-}yP_2O_7]^n$ complexes using N-chelating resins. J Hazard Mater 2020;398:122960.
[7] Nyström F, Nordqvist K, Herrmann I, Hedström A, Viklander M. Removal of metals and hydrocarbons from stormwater using coagulation and flocculation. Water Res 2020;182:115919.
[8] Wang Y, Pan T, Yu Y, Wu Y, Pan Y, Yang X. A novel peroxymonosulfate (PMS)-enhanced iron coagulation process for simultaneous removal of trace organic pollutants in water. Water Res 2020;185:116136.
[9] Wang T, Zhang L, Li C, Yang W, Song T, Tang C, et al. Synthesis of core–shell magnetic Fe_3O_4@poly(*m*-phenylenediamine) particles for chromium reduction and adsorption. Environ Sci Technol 2015;49(9):5654–62.
[10] Ji C, Wu D, Lu J, Shan C, Ren Y, Li T, et al. Temperature regulated adsorption and desorption of heavy metals to A-MIL-121: mechanisms and the role of exchangeable protons. Water Res 2021;189:116599.
[11] Zhao DL, Japip S, Zhang Y, Weber M, Maletzko C, Chung TS. Emerging thin-film nanocomposite (TFN) membranes for reverse osmosis: a review. Water Res 2020;173:115557.
[12] Nie G, Qiu S, Wang X, Du Y, Zhang Q, Zhang Y, et al. A millimeter-sized negatively charged polymer embedded with molybdenum disulfide nanosheets for efficient removal of Pb(II) from aqueous solution. Chin Chem Lett 2021;32(7):2342–6.
[13] Zhang J, Gu D, Yang Y, Zhang H, Chen H, Dai D, et al. Influence of particle size on laser absorption and scanning track formation mechanisms of pure tungsten powder during selective laser melting. Engineering 2019;5(4):736–45.
[14] Fang R, Lu C, Zhong Y, Xiao Z, Liang C, Huang H, et al. Puffed rice carbon with coupled sulfur and metal iron for high-efficiency mercury removal in aqueous solution. Environ Sci Technol 2020;54(4):2539–47.

[15] Wang T, Jiang Z, An T, Li G, Zhao H, Wong PK. Enhanced visible-light-driven photocatalytic bacterial inactivation by ultrathin carbon-coated magnetic cobalt ferrite nanoparticles. Environ Sci Technol 2018;52(8):4774–84.
[16] Guo J, Wan Y, Zhu Y, Zhao M, Tang Z. Advanced photocatalysts based on metal nanoparticle/metal–organic framework composites. Nano Res 2021;14(7):2037–52.
[17] Qu Z, Wu Y, Zhu S, Yu Y, Huo M, Zhang L, et al. Green synthesis of magnetic adsorbent using groundwater treatment sludge for tetracycline adsorption. Engineering 2019;5(5):880–7.
[18] Zhang G, Liu F, Liu H, Qu J, Liu R. Respective role of Fe and Mn oxide contents for arsenic sorption in iron and manganese binary oxide: an X-ray absorption spectroscopy investigation. Environ Sci Technol 2014;48(17):10316–22.
[19] Mendez JC, Hiemstra T. High and low affinity sites of ferrihydrite for metal ion adsorption: data and modeling of the alkaline-earth ions Be, Mg, Ca, Sr, Ba, and Ra. Geochim Cosmochim Acta 2020;286:289–305.
[20] Razanajatovo MR, Gao W, Song Y, Zhao X, Sun Q, Zhang Q. Selective adsorption of phosphate in water using lanthanum-based nanomaterials: a critical review. Chin Chem Lett. 2021;32(9):2637–47.
[21] Chekli L, Phuntsho S, Roy M, Lombi E, Donner E, Shon HK. Assessing the aggregation behaviour of iron oxide nanoparticles under relevant environmental conditions using a multi-method approach. Water Res 2013;47(13):4585–99.
[22] Lofrano G, Carotenuto M, Libralato G, Domingos RF, Markus A, Dini L, et al. Polymer functionalized nanocomposites for metals removal from water and wastewater: an overview. Water Res 2016;92:22–37.
[23] Qu X, Alvarez PJJ, Li Q. Applications of nanotechnology in water and wastewater treatment. Water Res 2013;47(12):3931–46.
[24] Ali Zadeh Sahraei O, Larachi F, Abatzoglou N, Iliuta MC. Hydrogen production by glycerol steam reforming catalyzed by Ni-promoted Fe/Mg-bearing metallurgical wastes. Appl Catal B 2017;219:183–93.
[25] Yang F, Zhang S, Sun Y, Cheng K, Li J, Tsang DCW. Fabrication and characterization of hydrophilic corn stalk biochar-supported nanoscale zero-valent iron composites for efficient metal removal. Bioresour Technol 2018;265:490–7.
[26] Jin H, Zhou H, Ji P, Zhang C, Luo J, Zeng W, et al. ZIF-8/$LiFePO_4$ derived Fe–N–P Co-doped carbon nanotube encapsulated Fe_2P nanoparticles for efficient oxygen reduction and Zn–air batteries. Nano Res 2020;13(3):818–23.
[27] Zhang Z, Tan Y, Zeng T, Yu L, Chen R, Cheng N, et al. Tuning the dual-active sites of ZIF-67 derived porous nanomaterials for boosting oxygen catalysis and rechargeable Zn–air batteries. Nano Res 2021;14(7):2353–62.
[28] Jiang Y, Hua M, Wu B, Ma H, Pan B, Zhang Q. Enhanced removal of arsenic from a highly laden industrial effluent using a combined coprecipitation/nano-adsorption process. Environ Sci Pollut Res Int 2014;21(10):6729–35.
[29] Hua M, Xiao L, Pan B, Zhang Q. Validation of polymer-based nano-iron oxide in further phosphorus removal from bioeffluent: laboratory and scaledup study. Front Environ Sci Eng 2013;7(3):435–41.
[30] Luo Z, Castleman AW, Khanna SN. Reactivity of metal clusters. Chem Rev 2016;116(23):14456–92.
[31] Liu JX, Wang P, Xu W, Hensen EJM. Particle size and crystal phase effects in Fischer–Tropsch catalysts. Engineering 2017;3(4):467–76.
[32] Yavuz CT, Mayo JT, Yu WW, Prakash A, Falkner JC, Yean S, et al. Low-field magnetic separation of monodisperse Fe_3O_4 nanocrystals. Science 2006;314(5801):964–7.
[33] Zhang X, Cheng C, Qian J, Lu Z, Pan S, Pan B. Highly efficient water decontamination by using sub-10 nm FeOOH confined within millimeter-sized mesoporous polystyrene beads. Environ Sci Technol 2017;51(16):9210–8.
[34] Qi Y, He CT, Lin J, Lin S, Liu J, Huang J, et al. Mild metal–organic-gel route for synthesis of stable sub-5-nm metal–organic framework nanocrystals. Nano Res 2017;10(11):3621–8.
[35] Zhang D, Wang Y, Deng J, Wang X, Guo G. Microfluidics revealing formation mechanism of intermetallic nanocrystals. Nano Energy 2020;70:104565.
[36] Zhang N, Yu SH, Abruña HD. Regulating lithium nucleation and growth by zinc modified current collectors. Nano Res 2020;13(1):45–51.
[37] Su X, Chang J, Wu S, Tang B, Zhang S. Synthesis of highly uniform Cu_2O spheres by a two-step approach and their assembly to form photonic crystals with a brilliant color. Nanoscale 2016;8(11):6155–61.
[38] Baronov A, Bufkin K, Shaw DW, Johnson BL, Patrick DL. A simple model of burst nucleation. Phys Chem Chem Phys 2015;17(32):20846–52.
[39] Xia Y, Xiong Y, Lim B, Skrabalak S. Shape-controlled synthesis of metal nanocrystals: simple chemistry meets complex physics? Angew Chem Int Ed Engl 2009;48(1):60–103.
[40] Jiang X, Shao Y, Sheng L, Li P, He G. Membrane crystallization for process intensification and control: a review. Engineering 2021;7(1):50–62.
[41] Jin R, Zeng C, Zhou M, Chen Y. Atomically precise colloidal metal nanoclusters and nanoparticles: fundamentals and opportunities. Chem Rev 2016;116(18):10346–413.
[42] Fernández-Lodeiro C, Fernández-Lodeiro J, Carbó-Argibay E, Lodeiro C, Pérez-Juste J, Pastoriza-Santos I. The versatility of Fe(II) in the synthesis of uniform citrate-stabilized plasmonic nanoparticles with tunable size at room temperature. Nano Res 2020;13(9):2351–5.
[43] Wu Z, Yang S, Wu W. Shape control of inorganic nanoparticles from solution. Nanoscale 2016;8(3):1237–59.
[44] Saldanha PL, Lesnyak V, Manna L. Large scale syntheses of colloidal nanomaterials. Nano Today 2017;12:46–63.
[45] Zhang Y, Kubů M, Mazur M, Čejka J. Synthesis of Pt-MWW with controllable nanoparticle size. Catal Today 2019;324:135–43.
[46] Gerber IC, Serp P. A theory/experience description of support effects in carbon-supported catalysts. Chem Rev 2020;120(2):1250–349.
[47] Zhang QX, Zhang ZP, Li AM, Pan BC, Zhang XL. Advance in ion exchange and adsorption resins in China. Acta Polym Sin 2018;7:814–28. Chinese.
[48] Topp NE, Pepper KW. Properties of ion-exchange resins in relation to their structure. Part I. Titration curves. J Chem Soc 1949:3299–303.
[49] Corain B, Jerabek K, Centomo P, Canton P. Generation of size-controlled Pd^0 nanoclusters inside nanoporous domains of gel-type resins: diverse and convergent evidence that supports a strategy of template-controlled synthesis. Angew Chem Int Ed Engl 2004;43(8):959–62.
[50] Zhang X, Wu M, Dong H, Li H, Pan B. Simultaneous oxidation and sequestration of As(III) from water by using redox polymer-based Fe(III) oxide nanocomposite. Environ Sci Technol 2017;51(11):6326–34.
[51] Zhang Y, She X, Gao X, Shan C, Pan B. Unexpected favorable role of Ca^{2+} in phosphate removal by using nanosized ferric oxides confined in porous polystyrene beads. Environ Sci Technol 2019;53(1):365–72.
[52] Pan B, Xu J, Wu B, Li Z, Liu X. Enhanced removal of fluoride by polystyrene anion exchanger supported hydrous zirconium oxide nanoparticles. Environ Sci Technol 2013;47(16):9347–54.
[53] Zhu L, Liu Y, Chen Ji. Synthesis of *n*-methylimidazolium functionalized strongly basic anion exchange resins for adsorption of Cr(VI). Ind Eng Chem Res 2009;48(7):3261–7.
[54] Sherrington DC. Preparation, structure and morphology of polymer supports. Chem Commun 1998;21:2275–86.
[55] Du Y, Fang P, Chen J, Hou X. Synthesis of reusable macroporous St/BMA copolymer resin and its absorbency to organic solvent and oil. Polym Adv Technol 2016;27(3):393–403.
[56] Sun S, Gebauer D, Cölfen H. Alignment of amorphous iron oxide clusters: a non-classical mechanism for magnetite formation. Angew Chem Int Ed Engl 2017;56(14):4042–6.
[57] Yao ZF, Wang ZY, Wu HT, Lu Y, Li QY, Zou L, et al. Ordered solid-state microstructures of conjugated polymers arising from solution-state aggregation. Angew Chem Int Ed Engl 2020;59(40):17467–71.
[58] Zheng S, Li Z, Liu Z. The fast homogeneous diffusion of hydrogel under different stimuli. Int J Mech Sci 2018;137:263–70.
[59] Pan S, Zhang X, Qian J, Lu Z, Hua M, Cheng C, et al. A new strategy to address the challenges of nanoparticles in practical water treatment: mesoporous nanocomposite beads via flash freezing. Nanoscale 2017;9(48):19154–61.
[60] Chernyshova IV, Ponnurangam S, Somasundaran P. Effect of nanosize on catalytic properties of ferric (hydr)oxides in water: mechanistic insights. J Catal 2011;282(1):25–34.
[61] Shi QT, Sterbinsky GE, Zhang SJ, Christodoulatos C, Korfiatis GP, Meng XG. Formation of Fe(III)–As(V) complexes: effect on the solubility of ferric hydroxide precipitates and molecular structural identification. Environ Sci Nano 2020;7(5):1388–98.
[62] Wei Y, Wei S, Liu C, Chen T, Tang Y, Ma J, et al. Efficient removal of arsenic from groundwater using iron oxide nanoneedle array-decorated biochar fibers with high Fe utilization and fast adsorption kinetics. Water Res 2019;167:115107.
[63] Li H, Shan C, Zhang Y, Cai J, Zhang W, Pan B. Arsenate adsorption by hydrous ferric oxide nanoparticles embedded in cross-linked anion exchanger: effect of the host pore structure. ACS Appl Mater Interfaces 2016;8(5):3012–20.
[64] Fang Z, Li Z, Zhang X, Pan S, Wu M, Pan B. Enhanced arsenite removal from silicate-containing water by using redox polymer-based Fe(III) oxides nanocomposite. Water Res 2021;189:116673.
[65] Uddin MJ, Jeong YK. Review: efficiently performing periodic elements with modern adsorption technologies for arsenic removal. Environ Sci Pollut Res Int 2020;27(32):39888–912.
[66] Zhang X, Zhang L, Li Z, Jiang Z, Zheng Q, Lin B, et al. Rational design of antifouling polymeric nanocomposite for sustainable fluoride removal from NOM-rich water. Environ Sci Technol 2017;51(22):13363–71.